PHYSICAL REVIEW A **83**, 023408 (2011)

Polarization-dependent atomic dipole traps behind a circular aperture for neutral-atom quantum computing

Katharina Gillen-Christandl* and Bert D. Copsey
Physics Department, California Polytechnic State University, San Luis Obispo, California 93407, USA
(Received 26 September 2010; published 9 February 2011)

The neutral-atom quantum computing community has successfully implemented almost all necessary steps for constructing a neutral-atom quantum computer. We present computational results of a study aimed at solving the remaining problem of creating a quantum memory with individually addressable sites for quantum computing. The basis of this quantum memory is the diffraction pattern formed by laser light incident on a circular aperture. Very close to the aperture, the diffraction pattern has localized bright and dark spots that can serve as red-detuned or blue-detuned atomic dipole traps. These traps are suitable for quantum computing even for moderate laser powers. In particular, for moderate laser intensities ($\sim$100 W/cm^2) and comparatively small detunings ($\sim$1000–10 000 linewidths), trap depths of $\sim$1 mK and trap frequencies of several to tens of kilohertz are achieved. Our results indicate that these dipole traps can be moved by tilting the incident laser beams without significantly changing the trap properties. We also explored the polarization dependence of these dipole traps. We developed a code that calculates the trapping potential energy for any magnetic substate of any hyperfine ground state of any alkali-metal atom for any laser detuning much smaller than the fine-structure splitting for any given electric field distribution. We describe details of our calculations and include a summary of different notations and conventions for the reduced matrix element and how to convert it to SI units. We applied this code to these traps and found a method for bringing two traps together and apart controllably without expelling the atoms from the trap and without significant tunneling probability between the traps. This approach can be scaled up to a two-dimensional array of many pinholes, forming a quantum memory with single-site addressability, in which pairs of atoms can be brought together and apart for two-qubit gates for quantum computing.

DOI: 10.1103/PhysRevA.83.023408 PACS number(s): 37.10.Gh, 03.67.Lx, 42.25.Ja, 42.50.Ct

I. INTRODUCTION

Neutral-atom quantum computing [1–4] is a promising avenue toward a full implementation of a quantum computer [5]. The internal electronic state of a neutral atom (or, in some cases, the motional state [6]) serves as the qubit. Usually the qubit states that are chosen are part of the ground-state manifold, resulting in long coherence times, limited by trap photon scattering or motional heating. Initialization, readout, and single-qubit rotations are achieved using well-established spectroscopic techniques. Recent advances have been made in trapping, manipulating, and reading out single atoms trapped in dipole traps [7,8]. Two-qubit gates have been experimentally demonstrated [9,10] using the dipole blockade, and entanglement between two qubits has also been achieved using cold collisions [11].

To scale this system up to many qubits, neutral atoms are most commonly trapped at the sites of a three-dimensional (3D) optical lattice. However, atoms trapped in 3D optical lattices cannot be addressed individually using focused laser beams, due to the 3D structure of the trap array, which limits the operations that can be performed on qubits trapped in 3D optical lattices. As a solution to this problem, several methods for creating two-dimensional (2D) arrays of atom traps have been proposed. Dumke *et al.* experimentally demonstrated a 2D array of atom traps formed behind an array of microlenses [12]. The distance between adjacent traps is determined by the center-to-center distance between the microlenses and thus can be designed to be large enough to address individual atoms with a focused laser beam. Recently, a scalable extension of this method was achieved using a spatial light modulator combined with an array of microlenses [13]. Other ideas using spatial light modulators (SLMs) [14,15], mirrors [16,17], Fresnel lenses [18], metamaterial lenses [19], or diffraction patterns [20,21] are being explored. Of particular interest are approaches that allow trapping atoms in dark spots, reducing the trap photon absorption probability, one of the major decoherence mechanisms in optical traps. Christandl *et al.* have proposed a 2D array of dark atom traps at intertrap distances of several microns, formed by blue-detuned evanescent waves above a waveguide [22]. Two-dimensional arrays of dark-spot traps can also be generated using a combination of a phase plate or grating and an array of microlenses [23,24]. The application of light fields near circular apertures of micron or nanometer sizes for trapping and control of cold atoms has been studied for some time [25–30]. Our approach, which uses diffraction at circular apertures of sizes exceeding the laser wavelength, offers a simple, versatile method for generating a 2D array of either dark-spot or bright-spot traps, depending on the laser detuning. In addition, two traps, including two dark-spot traps, can be brought together and apart without losing the atoms from the traps by utilizing the light polarization dependence of the trapping potential energy. Imaging of 2D arrays similar to the types described previously with single-site resolution has been demonstrated successfully [31], indicating that single-site addressing and readout are possible in 2D arrays.

Laser light incident on a circular aperture forms localized bright and dark spots in the region near the aperture, closer

*kgillen@calpoly.edu

than the usual near-field diffraction [32]. These bright and dark spots can serve as atomic dipole traps for red-detuned and blue-detuned light, respectively [33]. Moderate laser powers ($\sim$100 W/cm^2) and small detunings ($\sim$1000–10 000 linewidths) result in trap depths of $\sim$1 mK and trap frequencies of several to $\sim$10 kHz. These traps are theoretically suitable for storing atomic qubits.

In this paper, we describe how the light-polarization-dependent trapping potential energy [34] for any electric field pattern, for any alkali species, in any magnetic substate is calculated for any detuning small compared to the fine-structure splitting. Much simpler expressions for larger detunings are readily available in the literature [34,35]. We also discuss the normalization conventions encountered for the reduced matrix elements, as exact knowledge of these is needed to obtain the trapping potential energy in nonarbitrary units for direct comparison with experimental results. We then show computational results applying these expressions to the atomic dipole traps formed behind a circular aperture. We show that the traps stay intact upon tilting the incident laser beam, indicating the ability to move these atom traps. We show how the light polarization dependence of atomic dipole traps can be exploited to bring pairs of atoms (including those in blue-detuned traps) together and apart without losing the atoms from the trap. This may allow for the implementation of two-qubit gates with previously realized methods [9,10]. This approach can be scaled up to a 2D array of many circular apertures, with the trap distance determined by the center-to-center distance of the apertures, and therefore adjustable to a distance large enough to allow for resolving of individual atom sites with a focused laser beam for qubit manipulation.

Section II summarizes the theoretical background for the light-polarization-dependent atomic trapping potential-energy calculations. In Sec. III, we present our computational results on moving the atomic dipole traps formed behind a circular aperture and on bringing them together and apart. We also discuss how this approach can be scaled up to many qubits.

II. THEORY OF THE LIGHT POLARIZATION DEPENDENCE OF ATOMIC DIPOLE TRAPS

An electric field such as that from a laser induces an electric dipole moment in a neutral atom. In general, this induced dipole moment depends on the polarization of the laser light, as well as on the hyperfine level and Zeeman magnetic substate of the atom. The induced dipole moment due to a certain electric field is determined by the polarizability of the atom. The interaction of the induced dipole with the electric field of the laser light results in a potential energy and its associated force, which can trap the atom in regions of high or low light intensity. The potential-energy operator for the light atom interaction is given by [36]

$$\hat{U}(\mathbf{r}) = -\tfrac{1}{4}\mathbf{E}_0^*(\mathbf{r})\hat{\alpha}\mathbf{E}_0(\mathbf{r}). \tag{1}$$

Here, $\mathbf{E}_0(\mathbf{r})$ is the complex amplitude for an electric field written in the form $\mathbf{E}(\mathbf{r},t) = \mathrm{Re}[\mathbf{E}_0(\mathbf{r})e^{-i\omega t}]$, $\hat{\alpha}$ is the atomic polarizability tensor (for detailed discussions see [36,37]), and ω is the angular frequency of the laser light. Alternatively, the electric field is often written in its Fourier series form with positive and negative frequency components, $\mathbf{E}^{(+)} = \mathbf{E}_0^*/2$ and $\mathbf{E}^{(-)} = \mathbf{E}_0/2$, respectively,

$$\mathbf{E}(\mathbf{r},t) = \mathbf{E}^{(+)}(\mathbf{r})e^{-i\omega t} + \mathbf{E}^{(-)}(\mathbf{r})e^{i\omega t}. \tag{2}$$

The corresponding expression for the dipole potential-energy operator is then

$$\hat{U}(\mathbf{r}) = -\mathbf{E}^{(+)}(\mathbf{r})\hat{\alpha}\mathbf{E}^{(-)}(\mathbf{r}). \tag{3}$$

As derived in [34] and Appendix A, for an alkali atom, the polarizability tensor components in the spherical basis are

$$\hat{\alpha}_{q',q} = (-1)^{q'}\sum_{F'}\Bigg[\alpha_{0,F'F}f_{F'F}\sum_{m}\Big(c^{F,1,F'}_{m+q-q',q',m+q}c^{F,1,F'}_{m,q,m+q} \times |F,m+q-q'\rangle\langle F,m|\Big)\Bigg], \tag{4}$$

where $q',q = \pm1,0$ stands for the spherical basis components, $\alpha_{0,F'F}$ is the characteristic polarizability scalar, $f_{F'F}$ is the relative oscillator strength of the $F \to F'$ hyperfine transition, and the c's are the Clebsch-Gordan coefficient for the $F,m \to F',m+q$ dipole transition and a Clebsch-Gordan coefficient related to the $F',m+q \to F,m+q-q'$ dipole transition (see Appendix A), respectively. The relative oscillator strength of an $F \to F'$ transition is

$$f_{F'F} = (2J'+1)(2F+1)\left|\begin{Bmatrix} F' & I & J' \\ J & 1 & F \end{Bmatrix}\right|^2, \tag{5}$$

where the curly braces signify the six-J symbol and I is the quantum number for the nuclear spin of the atom. The characteristic polarizability scalar is given by

$$\alpha_{0,F'F} = -\frac{|\langle J'||d||J\rangle|^2}{\hbar\Delta_{F'F}}. \tag{6}$$

Here, $\Delta_{F'F}$ is the angular frequency detuning from the $F \to F'$ transition and $\langle J'||d||J\rangle$ is the reduced dipole matrix element for the $J \to J'$ fine-structure transition.

There are three common normalization conventions for the reduced dipole matrix element. A comparison of the three conventions, as well as an example for unit conversion of the reduced dipole matrix elements, are given in Appendix B.

In this work, we used the following relation (with the same normalization as [38]) for the polarizability scalar of an alkali atom to calculate the reduced matrix element [36]:

$$\alpha_{0,F'F} = -\frac{3\lambda^3}{32\pi^3}\frac{\Gamma}{\Delta_{F'F}}. \tag{7}$$

This equation is for the wavelength λ in centimeters and gives $\alpha_{0,F'F}$ in cgs units. In our work, we use SI units throughout our code, so we are also listing the SI version of this equation (i.e., with λ in units of meters),

$$\alpha_{0,F'F} = -\frac{3\lambda^3}{32\pi^3}\frac{\Gamma}{\Delta_{F'F}}1.11\times10^{-10}\frac{\mathrm{Jm}^2}{\mathrm{V}^2}. \tag{8}$$

In this study, we only present the diabatic potentials [39], which are the diagonal components of the potential-energy operator in the F, m_F basis. This is appropriate, because we plan on trapping precooled atoms in these traps, which will remain at the bottom of the potential-energy wells, rather than traveling through the wells. For the configurations that involve

movement of the traps, we need to consider two aspects of the speed of this motion. First, it must be slow compared to the trap frequency in order to reduce atom loss or state disturbance during motion. On the other hand, the motion should occur fast enough to reduce the probability of Raman transitions that could flip atoms into a different magnetic substate if the two atomic potential energies are very similar (e.g., when two traps are fully overlapped). Such Raman transitions can change the state of an atom into either an untrapped state or a state trapped by a different well (see Sec. III). As long as the Raman transition probability remains sufficiently low, we can use the diabatic potentials to describe the atom dynamics in our traps. To calculate the diabatic potential energy for a certain F, m_F state, we calculate the expectation value of the potential-energy operator as follows:

$$U_{F,m_F} = \langle F,m_F|\hat{U}|F,m_F\rangle. \tag{9}$$

Plugging in the dipole energy operator [Eq. (1)] explicitly, we get

$$\begin{aligned} U_{F,m_F} &= -\frac{1}{4}\sum_{q',q} E^*_{0q'}E_{0q}\hat{\alpha}_{q',q} \\ &= -\frac{1}{4}\sum_{q',q}\Bigg\{(-1)^{q'}E^*_{0q'}E_{0q}\sum_{F'}\Bigg[\alpha_{0,F'F}f_{F'F} \\ &\quad\times\sum_{m}\left(c^{F,1,F'}_{m+q-q',q',m+q}c^{F,1,F'}_{m,q,m+q}\right. \\ &\quad\left.\times\langle F,m_F|F,m+q-q'\rangle\langle F,m|F,m_F\rangle\right)\Bigg]\Bigg\}. \end{aligned} \tag{10}$$

Here, the $E_{0q',q}$ with $q',q = \pm 1,0$ are the spherical components of the electric field amplitude, corresponding to right and left circular light polarization, $\sigma^{\pm}$, and linear light polarization, π, respectively.

By exploiting orthonormality, this expression simplifies to

$$\begin{aligned} U_{F,m_F} &= -\frac{1}{4}\sum_{q}(-1)^q|E_{0q}|^2 \\ &\quad\times\sum_{F'}\alpha_{0,F'F}f_{F'F}\left(c^{F,1,F'}_{m_F,q,m_F+q}\right)^2. \end{aligned} \tag{11}$$

The electric field distributions for the diffraction pattern immediately behind a circular aperture were obtained using Hertz vector diffraction theory [40,41]. The diffraction code [42] yields the Cartesian components of the electric field. To find the spherical components, we use the spherical unit vectors [43]

$$\begin{aligned} \mathbf{e}_{-1} &= \frac{1}{\sqrt{2}}(\mathbf{e}_x - i\mathbf{e}_y) \\ \mathbf{e}_0 &= \mathbf{e}_z \\ \mathbf{e}_{+1} &= -\frac{1}{\sqrt{2}}(\mathbf{e}_x + i\mathbf{e}_y). \end{aligned} \tag{12}$$

Here, $\mathbf{e}_x$, $\mathbf{e}_y$, and $\mathbf{e}_z$ are the Cartesian unit vectors. From this, we find the spherical components of the complex amplitude of the electric field defined by

$$\begin{aligned} \mathbf{E}_0 &= E_{0x}\mathbf{e}_x + E_{0y}\mathbf{e}_y + E_{0z}\mathbf{e}_z \\ &= E_{0-1}\mathbf{e}_{-1} + E_{00}\mathbf{e}_0 + E_{0+1}\mathbf{e}_{+1}. \end{aligned} \tag{13}$$

Here E_{0j} for $j = x,y,z$ are the Cartesian components of the electric field amplitude. The spherical and Cartesian components are related by

$$\begin{aligned} E_{0-1} &= \frac{1}{\sqrt{2}}(E_{0x} + iE_{0y}), \\ E_{00} &= E_{0z}, \\ E_{0+1} &= \frac{1}{\sqrt{2}}(-E_{0x} + iE_{0y}). \end{aligned} \tag{14}$$

These spherical components were then plugged into Eq. (11).

Equations (5), (8), (11), and (14) were used to calculate the computational results presented in the next section. The computations were performed using a code [44] that will take any arbitrary electric field distribution in Cartesian coordinates, decompose it into its spherical components, and then calculate both the diabatic and adiabatic potentials for any given detuning $\Delta \ll \Delta_{\rm fs}$, where $\Delta_{\rm fs}$ denotes the fine-structure splitting of the excited state. Note that the detuning can be made arbitrarily small, including smaller than the excited-state hyperfine splitting. For larger detunings, the expressions simplify tremendously, as only the fine-structure splitting needs to be considered [34,35]. Also note that the E_{0j} are complex, so both the real and imaginary components must be supplied for this calculation. Appendix C shows the details of our specific electric field configurations (single laser beam incident at an angle and a pair of oppositely circularly polarized laser beams incident at an angle). The code has two variable input parameters: the laser detuning Δ from the transition $F \rightarrow$ maximum F', which is contained in $\Delta_{F'F}$, and the laser intensity I_0. The electric field amplitude at the aperture for each of the incident beams starts out normalized to 1. To change this to meaningful units, we insert the scaling due to intensity and convert the units of the potential energy from joules to millikelvin as follows:

$$U_{F,m_F}(\text{mK}) = 1000\frac{2}{3k_{\rm B}}\frac{2I_0}{\epsilon_0 c}U_{F,m_F}. \tag{15}$$

Here, the factor of 1000 is for converting kelvin to millikelvin, the factor of $\frac{2}{3k_{\rm B}}$ is for conversion from joules to Kelvin, and the factor of $\frac{2I_0}{\epsilon_0 c}$ is for inserting physical units for the electric field. For an intensity in W/m^2, this yields electric field units of volts per meter. Also, $k_{\rm B}$ is Boltzmann's constant, ϵ_0 is the permittivity of free space, and c is the speed of light. This is how we obtained the numerical results presented in the next section.

III. COMPUTATIONAL RESULTS FOR ATOM TRAPS BEHIND A CIRCULAR APERTURE

A. Movable atomic dipole traps

Consider the diffraction pattern resulting from a laser beam incident on a circular aperture at an angle of $\gamma = 0.055$ rad as shown in Fig. 1. Depending on the laser detuning, 3D atom traps will form in either the localized bright spots or dark spots of this diffraction pattern very close to the aperture. Figure 1(c) shows the diabatic trapping potential energy [calculated from the electric field distribution using Eq. (11)] for the $F = 1$, $m_F = 0$ magnetic substate of ^{87}Rb, for a laser intensity of 364 W/cm^2 and a laser detuning of $-10\,000\,\Gamma$ (red detuning)

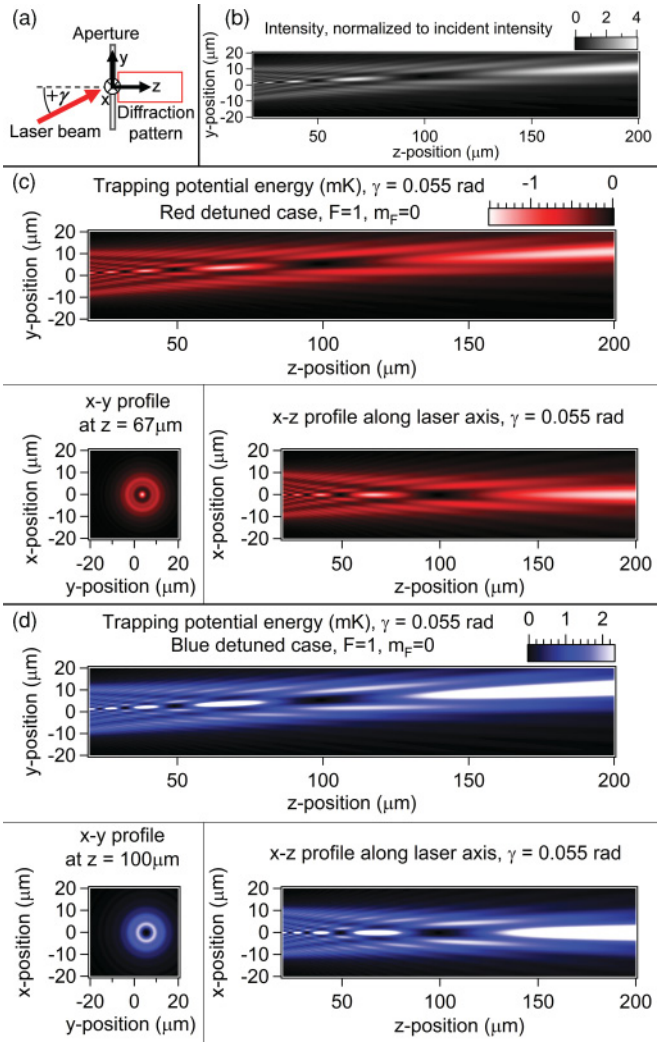

FIG. 1. (Color online) Diabatic trapping potential energy for a single laser beam (σ^+ polarization was used) incident on a circular aperture at an angle of $\gamma = 0.055$ rad. (a) Diagram of setup. (b) Intensity pattern. (c) Trapping potential energy for the light-polarization-independent $F = 1$, $m_F = 0$ magnetic substate of ^{87}Rb, for a laser intensity of 364 W/cm^2 and a laser detuning of $-10\,000$ Γ. (d) Trapping potential energy for the $F = 1$, $m_F = 0$ magnetic substate of ^{87}Rb, for a laser intensity of 116 W/cm^2 and a laser detuning of 1000 Γ.

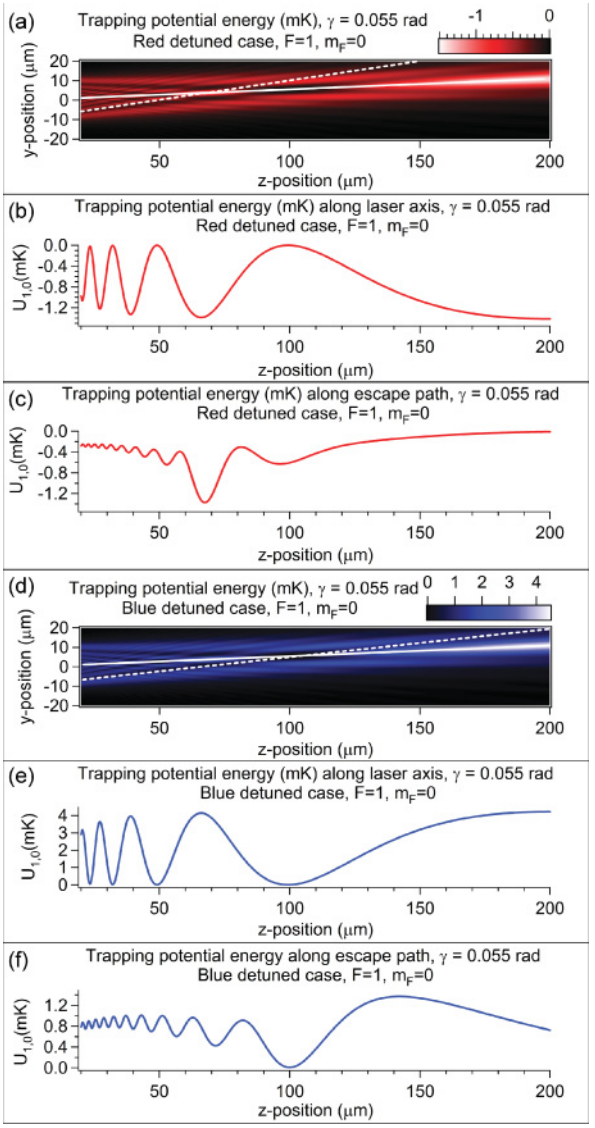

FIG. 2. (Color online) Diabatic trapping potential energy along the laser axis and along the paths of weakest confinement ("escape paths") for red-detuned and blue-detuned traps, for a single laser beam (σ^+ polarization was used) incident at $\gamma = 0.055$ rad, for the light-polarization-independent $F = 1$, $m_F = 0$ magnetic substate of ^{87}Rb. (a) Axial path (solid line) and escape path (dashed line) for a laser intensity of 364 W/cm^2 and a laser detuning of $-10\,000$ Γ. (b) Trapping potential energy along the laser axis for red-detuned trap [solid line in (a)]. (c) Trapping potential energy along the escape path for red-detuned trap [dashed line in (a), weakest trap direction]. (d) Axial path (solid line) and escape path (dashed line) for a laser intensity of 116 W/cm^2 and a laser detuning of 1000 Γ. (e) Trapping potential energy along the laser axis for the blue-detuned trap [solid line in (b)]. (f) Trapping potential energy along the escape path for the blue-detuned trap [dashed line in (b), weakest trap direction].

from the Rb D_2 transition ($\lambda = 780$ nm). The D_2 linewidth of Rb is $\Gamma = 2\pi \times 6$ MHz [43]. Atoms are trapped in the bright spots on the laser beam axis. Similarly, Fig. 1(d) shows the diabatic trapping potential energy for the $F = 1$, $m_F = 0$ magnetic substate of ^{87}Rb, for a laser intensity of 116 W/cm^2 and a laser detuning of 1000 Γ (blue detuning) from the Rb D_2 transition. Here, localized atom traps form in the dark spots on the laser beam axis.

We analyzed the properties of the traps formed farthest from the aperture ($z = 67$ μm for the farthest, well-localized bright spot for the red-detuned case and $z = 100$ μm for the blue-detuned case) and compared them to the normal incidence case. We chose these traps because they are biggest and most easily accessible for initial experiments. The traps formed closer to the aperture are also viable and, in fact, advantageous for quantum computing as they have larger trap frequencies. To determine the trap frequencies, we approximated the bottom of the (nonharmonic) traps with a harmonic oscillator potential-energy well. The values of the trap frequencies obtained depend on the fit range used. In this work, we chose a fit range of the bottom 200 μK of the well, unless otherwise stated.

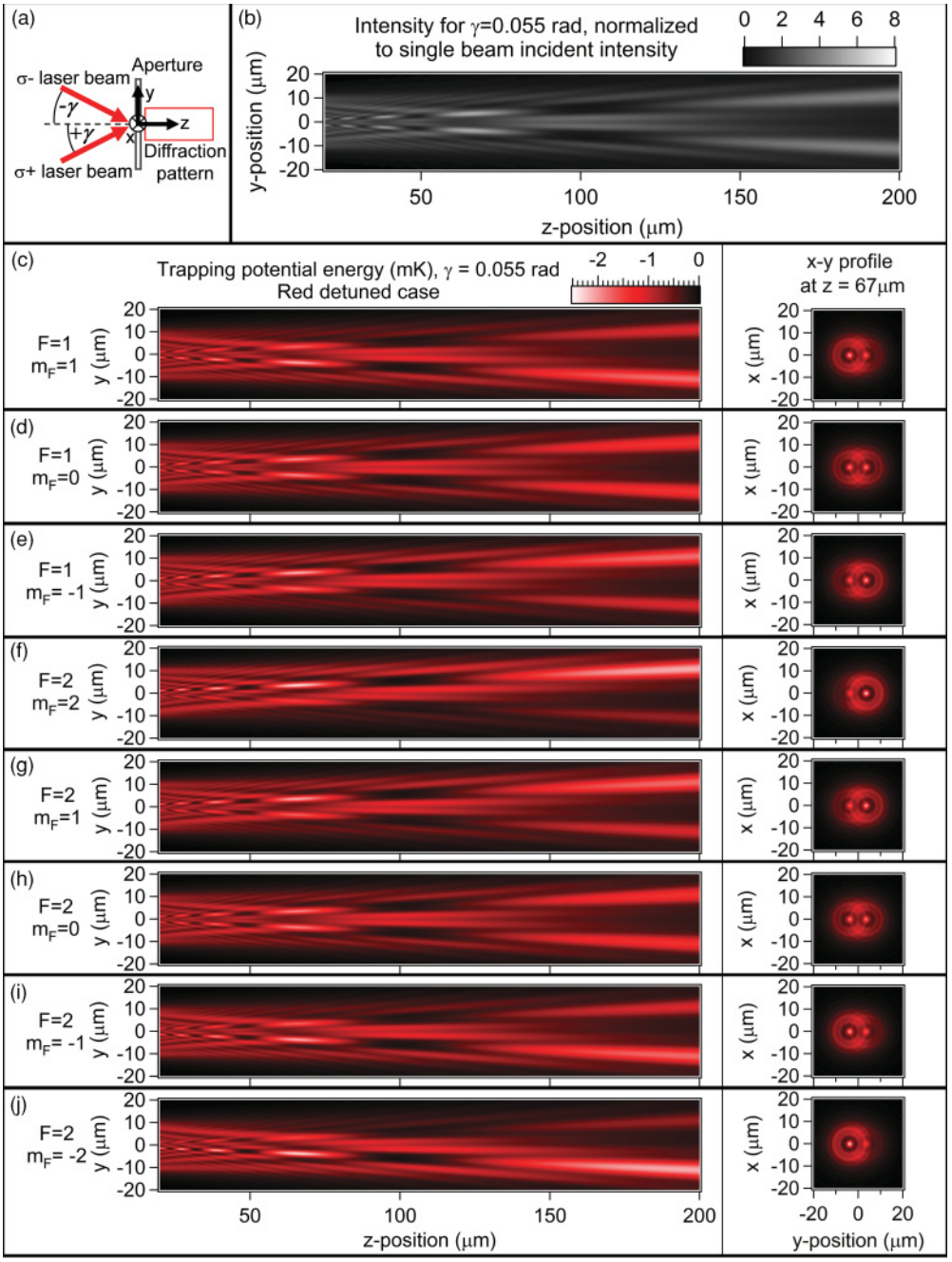

FIG. 3. (Color online) Diabatic trapping potential energy for two laser beams of opposite circular polarization incident on a circular aperture at an angle of $\gamma = 0.055$ rad. (a) Diagram of setup. (b) Intensity pattern, normalized to the incident intensity of one incident circularly polarized laser beam. (c)–(j) Trapping potential energy of the intensity pattern in (b) for the eight magnetic substates of the hyperfine ground-state manifold in ^{87}Rb for a laser intensity of 364 W/cm^2 and a laser detuning of $-10\,000\,\Gamma$ from the transitions from the respective F states.

Other trap properties of relevance for quantum information applications are the size of the motional harmonic oscillator ground-state wave function along a spatial dimension j,

$$\beta_j = \sqrt{\frac{\hbar}{2\pi f_j m_{\mathrm{Rb}}}}, \tag{16}$$

for the $1/e$ half-width of the probability density, and the energy difference $\Delta U_j \equiv h f_j / k_{\mathrm{B}}$ between two motional states of the potential-energy well. Here, f_j is the trap frequency along spatial dimension j, and m_{Rb} is the mass of one ^{87}Rb atom. We denote the spatial dimensions of the trap with indices $j = r_x$ for the radial dimension along x in the coordinate system of Fig. 1(a), $j = r_{yz}$ for the radial dimension in the y-z plane, and $j =$ axial for the axial dimension of the trap. In addition, the coherence of qubits in dipole traps is often limited by the scattering rate of trap photons. For blue-detuned traps with zero intensity at the bottom, the scattering rate for a ground-state atom (averaged over the extent of the wave function) can be written as [45]

$$\eta = \frac{\pi}{2}\left(f_{r_x} + f_{r_{yz}} + f_{\mathrm{axial}}\right)\frac{\Gamma}{\Delta}. \tag{17}$$

TABLE I. Trap properties for all F, m_F hyperfine ground states in ^{87}Rb for the red-detuned ($I_0 = 364$ W/cm^2, $\Delta = -10\,000\ \Gamma$) and blue-detuned ($I_0 = 116$ W/cm^2, $\Delta = 1000\ \Gamma$) examples. For trap frequencies, ground-state sizes, and energy differences, values are given in the order r_x, r_{yz}, axial. ΔU_{trap} denotes the trap depth.

	Red detuned					Blue detuned				
State F,m_F	f (kHz)	β (nm)	ΔU_j (μK)	η (kHz)	ΔU_{trap} (mK)	f (kHz)	β (nm)	ΔU_j (μK)	η (kHz)	ΔU_{trap} (mK)
1,1	83, 86, 8.1	37, 37, 120	4, 4.1, 0.39	42	1.2	27, 37, 6	65, 56, 140	1.3, 1.8, 0.29	0.11	1.2
1,0	74, 79, 7.5	40, 38, 120	3.6, 3.8, 0.36	38	0.98	26, 35, 5.3	67, 58, 150	1.2, 1.7, 0.26	0.10	1.0
1, -1	83, 86, 8.1	37, 37, 120	4, 4.1, 0.39	42	1.2	27, 37, 6	65, 56, 140	1.3, 1.8, 0.29	0.11	1.2
2,2	90, 92, 8.7	36, 36, 120	4.4, 4.4, 0.42	46	1.5	29, 41, 6.8	63, 53, 130	1.4, 2, 0.33	0.12	1.5
2,1	83, 86, 8.1	38, 37, 120	4, 4.1, 0.39	42	1.2	28, 38, 6.2	65, 55, 140	1.3, 1.8, 0.3	0.11	1.3
2,0	74, 79, 7.5	40, 38, 120	3.6, 3.8, 0.36	37	0.98	26, 35, 5.4	67, 58, 150	1.2, 1.7, 0.26	0.10	1.1
2, -1	83, 86, 8.1	38, 37, 120	4, 4.1, 0.39	42	1.2	28, 38, 6.2	65, 55, 140	1.3, 1.8, 0.3	0.11	1.3
2, -2	90, 92, 8.7	36, 36, 120	4.4, 4.4, 0.42	46	1.5	29, 41, 6.8	63, 53, 130	1.4, 2, 0.33	0.12	1.5

For red-detuned traps, a conservative estimate of the scattering rate is the peak scattering rate [35]

$$\eta = \frac{\Gamma}{\Delta\hbar} U_{\min}, \tag{18}$$

where $U_{\min}$ is the potential energy at the intensity peak of the trap. We determined the trap depth ΔU_{trap} by finding the peak potential energy of the path of weakest confinement ("escape path") with respect to the potential energy of the bottom of the well.

We determined that the trap properties calculated in [33] for normal incidence stay largely intact when the laser is incident at an angle. For comparisons to [33], we must mention that the trap frequencies cited there are for a harmonic fit range of 1 mK, whereas in this work we cite trap frequencies for 200 μK, which we deemed the relevant range for an atom sample precooled in a magneto-optical trap. The corresponding normal incidence frequencies for the red-detuned example are a radial trap frequency of $f_{r_x} = f_{r_{yz}} = 71$ kHz and an axial trap frequency of $f_{\text{axial}} = 6.9$ kHz. The other trap properties are $\beta_{r_x} = \beta_{r_{yz}} = 40$ nm, $\beta_{\text{axial}} = 130$ nm, $\Delta U_{r_x} = \Delta U_{r_{yz}} = 3.4$ μK, and $\Delta U_{\text{axial}} = 0.33$ μK. The trap-photon scattering rate is 27 kHz. The trap depth is 1 mK. Similarly, for blue-detuned light at normal incidence, we have $f_{r_x} = f_{r_{yz}} = 28$ kHz, $f_{\text{axial}} = 5.6$ kHz, $\beta_{r_x} = \beta_{r_{yz}} = 64$ nm, $\beta_{\text{axial}} = 140$ nm, $\Delta U_{r_x} = \Delta U_{r_{yz}} = 1.3$ μK, and $\Delta U_{\text{axial}} = 0.27$ μK. For the blue-detuned traps, the deviation from a harmonic potential-energy well is particularly pronounced, with the bottom being very flat. To fully describe these traps, we performed fits for a fit range of 20 μK, yielding fits valid only for very-low-temperature atoms (<1 μK) such as for atoms loaded from a Bose-Einstein condensate. The radial trap frequency for the bottom of the well for normal incidence is approximately 10 kHz and thus is comparable to the axial trap frequency (as are the other properties, $\beta_{r_x} = \beta_{r_{yz}} = 0.11$ μm, $\Delta U_{r_x} = \Delta U_{r_{yz}} = 0.48$ μK). A conservative estimate (using the larger trap frequencies) for the scattering rate is 97 Hz. The trap depth is 1 mK.

Figure 2 shows the trapping potential-energy curves along the laser beam direction, as well as along the direction of weakest confinement for both the red- and blue-detuned examples listed previously. For a beam incident at an angle of $\gamma = 0.055$ rad, for the red-detuned example (laser beam intensity of 364 W/cm^2, laser detuning of $-10\,000\ \Gamma$), we find a trap depth of 1 mK, $f_{r_x} = f_{r_{yz}} = 74$ kHz, $f_{\text{axial}} = 6.8$ kHz, $\beta_{r_x} = \beta_{r_{yz}} = 40$ nm, $\beta_{\text{axial}} = 130$ nm, $\Delta U_{r_x} = \Delta U_{r_{yz}} = 3.6$ μK, and $\Delta U_{\text{axial}} = 0.33$ μK. The average scattering rate is 27 kHz. These results are very similar to those for normal incidence. For the blue-detuned example (laser beam intensity of 116 W/cm^2, laser detuning of $1000\ \Gamma$), we find a trap depth of 0.9 mK, $f_{r_x} = f_{r_{yz}} = 26$ kHz, $f_{\text{axial}} = 5.5$ kHz, $\beta_{r_x} = \beta_{r_{yz}} = 67$ nm, $\beta_{\text{axial}} = 150$ nm, $\Delta U_{r_x} = \Delta U_{r_{yz}} = 1.3$ μK, and $\Delta U_{\text{axial}} = 0.26$ μK. The radial frequencies describing the behavior of the bottom of the blue well are $f_{r_x} = 5.6$ kHz and $f_{r_{yz}} = 6.7$ kHz, with $\beta_{r_x} = 140$ nm, $\beta_{r_{yz}} = 130$ nm, $\Delta U_{r_x} = 0.27$ μK, and $\Delta U_{r_{yz}} = 0.32$ μK. At this level, we are starting to notice differences between the untilted x direction and the dimension with tilt (y-z plane). Again, these results are very close to the normal incidence values. Therefore, the traps stay intact upon tilting.

Thus, by tilting the incident laser beam, an atom trapped at a bright spot or dark spot can be moved. We propose using this to bring two qubits together and apart by employing two laser beams at an angle, as shown in Fig. 3. One atom is placed in each of the two bright-spot traps (for red-detuned light) or dark-spot traps (for blue-detuned light). The laser beams are then tilted together to overlap the atoms for two-qubit quantum operations and tilted apart to separate the atoms.

There are several issues with this approach. When overlapping the wells, there is a significant probability for the atoms to tunnel between the traps and switch places. This is detrimental for quantum computing. In addition, for blue-detuned traps, the wall from one trap will push the atom out of the other trap. Both of these issues can be addressed by exploiting the light polarization dependence of the trapping potential energy for atoms in different magnetic substates, as discussed in the next section.

B. Atomic trapping potential energy for different magnetic substates

Because of the dependence of the trapping potential energy on the light polarization and the magnetic substate of a trapped atom as outlined in Sec. II, atoms in different magnetic

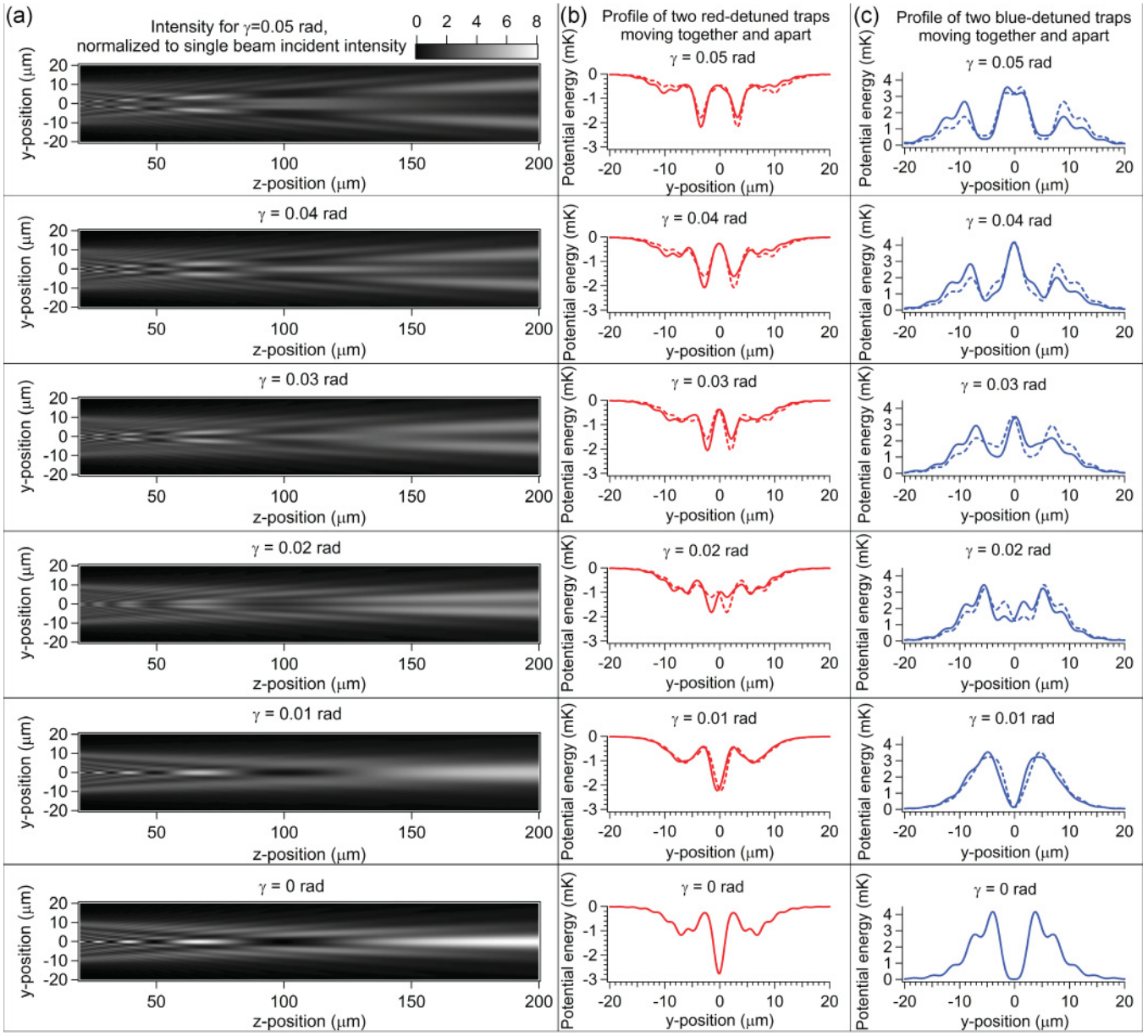

FIG. 4. (Color online) Bringing two traps together. (a) Column showing the intensity pattern, normalized to the incident intensity of one incident circularly polarized laser beam, for several incident angles γ. (b) Column showing the diabatic potential-energy profile along the y direction at $z = 67$ μm for the $F = 1$, $m_F = 1$ (solid line) and $m_F = -1$ (dashed line) magnetic substates of ^{87}Rb trapped in the intensity pattern from (a) for several incident angles γ, a laser intensity of 364 W/cm^2, and a laser detuning of $-10\,000$ Γ. (c) Column showing the diabatic potential-energy profile along the y direction at $z = 100$ μm for the $F = 1$, $m_F = 1$ (solid line) and $m_F = -1$ (dashed line) magnetic substates of ^{87}Rb trapped in the intensity pattern from (a) for several incident angles γ, a laser intensity of 116 W/cm^2, and a laser detuning of 1000 Γ.

substates placed in the same light pattern have a different trapping potential-energy curve. Consider the configuration in Fig. 3. A right-circularly polarized (σ^+) laser beam and a left-circularly polarized (σ^-) laser beam are incident on a circular aperture at angles γ and $-\gamma$, respectively. Figure 3(b) shows the intensity pattern for an incident angle of $\gamma = 0.055$ rad. We chose this angle as an example, as the trap sites examined here are well separated for this angle. Figures 3(c)–3(j) show the diabatic trapping potential energy for the eight magnetic substates of the ^{87}Rb hyperfine ground-state manifold, for the red-detuned example. The results are for a laser detuning of $\Delta = -10\,000$ Γ from the $F = 1 \rightarrow F' = 3$ transition and from the $F = 2 \rightarrow F' = 3$ transition, respectively. Table I summarizes the trap properties for both the red-detuned trap formed by the well-localized bright spot farthest from the aperture ($z = 67$ μm) and the blue-detuned trap formed by the dark spot farthest from the aperture ($z = 100$ μm). Note that only the 200-μK fit results are shown. For blue-detuned traps, the properties of the bottom of the well are better approximated with a 20-μK fit. For the x direction, this yields trap properties comparable to the axial trap properties listed. For the y-z plane, a miniwell is formed at the bottom of the major well and has

trap properties comparable to the radial trap properties listed in the table. The polarization dependence of the potential energy for each magnetic substate is evident. For both examples, we chose a detuning that is large compared to the excited-state hyperfine splitting, and thus there is very little dependence of the detuning on F' during the F' summation in Eq. (11). Also, the results shown are for the same detuning from the F to F' transition for both $F = 1$ and $F = 2$, so the differences in the potential energies are mostly due to the magnetic substate and the light polarization.

One consequence of this polarization dependence of the potential energy for use in quantum computing is the following. As can be seen in Fig. 3(c), we find that an atom (qubit) in the $F = 1$, $m_F = 1$ substate experiences strong confinement in all dimensions in the bright spot from the σ^- beam (i.e., the bottom or left bright spot in the y-z or x-y profile, respectively), at $z = 67$ μm from the aperture. While the bright spot due to the σ^+ beam (top or right bright spot in the y-z or x-y profile, respectively) is also confined in all dimensions, the confinement is significantly weaker due to the polarization dependence of the potential energy. Therefore, a $F = 1, m_F = 1$ atom, seeking the location of lowest potential energy is trapped in the σ^- bright spot. Similarly, as visible in Fig. 3(e), an atom in the $F = 1, m_F = -1$ substate is trapped in the σ^+ bright spot. Consequently, both atoms (qubits) can be stored in separate locations within the same light pattern, shown in Fig. 3(b). A similar polarization dependence effect has been successfully demonstrated in 3D optical lattices [46].

C. Bringing atom traps together and apart for two-qubit operations

1. Red-detuned diffraction trap

Figure 4 shows the trapping potential-energy plots for an atom in the $F = 1, m_F = 1$ substate, trapped in the σ^- beam, and an atom in the $F = 1, m_F = -1$ substate, trapped in the σ^+ beam of Fig. 3(a), for several angles. Figure 4(a) depicts the intensity pattern created by the setup from Fig. 3(a) for several angles, and Fig. 4(b) shows the potential-energy profile along the y direction, at the location of the primary red-detuned trap, $z = 67$ μm, for a pair of 364-W/cm^2 laser beams with opposite circular polarization, tuned 10 000 linewidths to the red of the ^{87}Rb D_2 transition.

Figure 4(b) demonstrates that for the red-detuned case the two traps move together continuously as the lasers are tilted to normal incidence, at which point the two traps are completely overlapped. This process can be reversed by tilting the laser beams apart. Each atom will be most probable to follow its trap as there is a difference in trapping strength between the two traps, due to the light polarization dependence. For instance, an atom in state $F = 1$, $m_F = 1$, trapped in the primary bright spot of the normal incidence configuration, follows the solid potential-energy curve toward the negative y direction in Fig. 4(b) as the angle γ of the two beams is slowly increased. By the same means, an atom in $F = 1$, $m_F = -1$ remains in the dashed potential-energy minimum, moving toward the positive y direction as the two beams are separated. In this way, we can bring two atoms together and apart without experiencing significant trap or tunneling losses.

The major source of tunneling in this setup is due to trap photon Raman transitions when the potential-energy curves for both atoms (i.e., both states) cross, for example, when the wells are completely overlapped. The probability of such a transition can be reduced by performing this operation significantly faster than the Raman scattering rate.

2. Blue-detuned diffraction trap

Figure 4(c) shows the corresponding trapping potential-energy profiles at the location of the primary blue-detuned trap, $z = 100$ μm, for a pair of 116-W/cm^2 laser beams with opposite circular polarization, tuned 1000 linewidths to the blue of the ^{87}Rb D_2 transition.

Since for blue-detuned light atoms are trapped in dark spots, it may generally be desirable to use blue-detuned traps for quantum computing to ensure long decoherence times. As illustrated in Fig. 4(a), as the two beams are moved together and apart, an intensity wall moves through the dark spot of each beam. However, as can be seen in Fig. 4(c), the associated potential energy of the intensity wall is not large enough to push the atoms out of the trap. Thus, the two atoms can still be overlapped completely, without switching wells, as the σ^- well traps the $F = 1, m_F = 1$ atom more strongly than the σ^+ well, and vice versa.

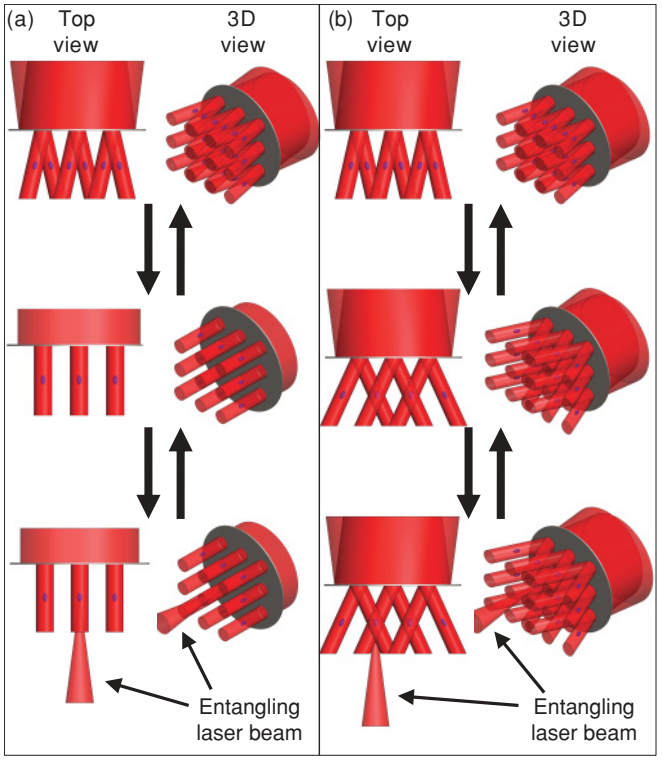

FIG. 5. (Color online) A 2D array of diffraction traps behind a 2D array of circular apertures. For appropriate aperture spacings, e.g., a few microns, individual trap sites can be addressed with a focused laser beam. Two atoms are brought together by tilting the incident laser beams, entangled with a focused laser beam, and moved apart by tilting the laser beams back. (a) Laser beams are tilted to normal incidence, bringing two traps from the same aperture together. (b) Laser beam tilt is increased, bringing two traps from neighboring apertures together.

However, the potential wall will influence the motion of the atom. For quantum computing, this disturbance must be kept negligible or must be reversible to avoid deterioration of the computation. If this is not possible, the advantages of trapping the atoms in locations of low light intensity are erased by the disturbance due to this potential-energy wall, and trapping in the bright spots with sufficiently large detuning may be preferable.

3. Scaling up to many traps

The approach presented here can be scaled up to a large array of circular apertures illuminated by a pair of laser beams, as shown in Fig. 5. Each aperture has the previously described potential-energy patterns behind it, so each aperture can trap one atom in each of the two traps that are formed. The distance between adjacent pairs of traps is equal to the distance between the apertures, and the distance between individual atoms is further controlled by the tilting angle of the laser beams. By making aperture arrays with a few microns between apertures, individual trap sites can be resolved by a focused laser beam. By tilting the laser beams to normal incidence and back, as shown in Fig. 5(a), we can bring all pairs of atoms together and apart simultaneously, and either perform large-scale parallel quantum operations or address individual pairs to entangle them. By tilting the laser beam farther, we can bring pairs of atoms from neighboring apertures together and entangle them, as shown in Fig. 5(b). This opens up the possibility of creating a fully functional quantum memory with individually addressable sites and the ability to bring pairs of qubits together and apart.

IV. CONCLUSIONS

We have computationally explored the feasibility of using an array of circular apertures to store qubits for quantum computing. We developed a code that allows the computation of the potential-energy curve for any electric field distribution, any magnetic substate of any alkali atom, and any laser detuning that is much smaller than the excited-state fine-structure splitting. Using this code, we determined that dipole traps formed in the diffraction pattern immediately behind a circular aperture can be moved by tilting the incident laser beam, without significantly changing or diminishing the trap properties. This allows moving atoms trapped in these patterns. Furthermore, we showed that by exploiting the light polarization dependence of the potential energy, two atoms in different magnetic substates trapped in two laser beams of opposite circular polarization can be brought together and apart by tilting the laser beams, without expelling the atoms and without significant probability of tunneling. This may be used to facilitate entangling two-qubit operations, such as the gates demonstrated in [9,10]. This method can be scaled up to a 2D array of many apertures. The distance between individual qubits is determined by the distance between adjacent apertures as well as the laser beam tilt, so it can be designed such that single-site resolution with a focused laser beam is possible. It is thus possible to create a 2D array of qubits that are individually addressable and can be brought together and apart for two qubit operations. In this work we have examined the basic principle and feasibility of this kind of qubit array. We look forward to exploring the limits and possibilities of this approach (e.g., maximum tilt angle to reach beyond immediate neighbors, minimum aperture size, use of multiple layers of traps) in future work.

ACKNOWLEDGMENTS

We thank Glen D. Gillen for providing the electric field data for diffraction at a circular aperture. We also thank Thomas D. Gutierrez, Ivan H. Deutsch, and Marianna S. Safronova for helpful discussions. This work was supported by the Department of the Navy, Office of Naval Research, Grant Nos. N00014-06-1-1111, N00014-07-1-1152, and N00014-08-1-1209, and National Science Foundation Grant No. PHY-0855524.

APPENDIX A: DERIVATION OF THE ATOMIC POLARIZABILITY TENSOR COMPONENTS

The spherical components of the polarizability tensor for an alkali atom of nuclear spin I, in a given hyperfine ground state F (with total angular momentum J) coupled to an excited-state hyperfine manifold with states F' (with angular momentum J') are derived in Appendix A of [34]. In this section, we show additional steps to supplement their derivation. We start from Eq. (A1) of [34],

$$\begin{aligned}\hat{\alpha}_{q',q} = -\sum_{F',m}\Bigg[&\frac{1}{\hbar\Delta_{F'F}}|F,m+q-q'\rangle \\ &\times\langle F,m+q-q'|\hat{d}_{-q'}|F',m+q\rangle \\ &\times\langle F',m+q|\hat{d}_q|F,m\rangle\langle F,m|\Bigg],\end{aligned} \tag{A1}$$

where $\hat{d}$ is the dipole transition operator and q',q correspond to the light polarization components. We can rewrite the two matrix elements using the Wigner-Eckart theorem in the Rose convention (Eq. (5.14) of [38], see Appendix B and Table II) as

$$\begin{aligned}\langle F,m+q-q'|\hat{d}_{-q'}|F',m+q\rangle &= c^{F',1,F}_{m+q,-q',m+q-q'}\langle F||d||F'\rangle, \\ \langle F',m+q|\hat{d}_q|F,m\rangle &= c^{F,1,F'}_{m,q,m+q}\langle F'||d||F\rangle.\end{aligned} \tag{A2}$$

For a more compact expression, it is useful to recast $\langle F||d||F'\rangle$ in terms of the complex conjugate of $\langle F'||d||F\rangle$ using Eq. (C.85) from [49], as well as the relationship between the Racah and Rose conventions for the reduced matrix element (see Appendix B and Table II),

$$\langle F||d||F'\rangle = (-1)^{F'-F}\sqrt{\frac{2F'+1}{2F+1}}\langle F'||d||F\rangle^*. \tag{A3}$$

This yields

$$\begin{aligned}\hat{\alpha}_{q',q} = -\sum_{F',m}\Bigg[&\frac{1}{\hbar\Delta_{F'F}}c^{F',1,F}_{m+q,-q',m+q-q'}c^{F,1,F'}_{m,q,m+q} \\ &\times(-1)^{F'-F}\sqrt{\frac{2F'+1}{2F+1}} \\ &\times|\langle F'||d||F\rangle|^2|F,m+q-q'\rangle\langle F,m|\Bigg].\end{aligned} \tag{A4}$$

TABLE II. Symbols and conventions for Clebsch-Gordan coefficients and reduced matrix elements from several sources. In the last row, we define the variable R to be the reduced matrix element of Rose [38].

Quantity	Condon-Shortley [47]	Racah [48]	Messiah [49]	Edmonds [50]	Rose [38]	This work[a]
Final-state quantum no.						
Principal	α	α	τ	γ'	(omitted)	(omitted)
Angular momentum	j	j	J	j'	j'	J'
Magnetic	m	m	M	m'	m'	m'
Initial-state quantum no.						
Principal	α'	α'	τ'	γ	(omitted)	(omitted)
Angular momentum	$j+1, j-1, j$	j'	J'	j	j	J
Magnetic	$m+1, m-1, m$	m'	M'	m	m	m
Rank of operator	1	k	k	k	L	k
Operator	T	$T^{(k)}$	$\mathbf{T}^{(k)}$	$\mathbf{T}(k)$	T_L	$T^{(k)}$
Component of operator	$\frac{1}{2}(\hat{i} \pm i\hat{j}), \hat{k}$	$T_q^{(k)}$	$T_q^{(k)}$	$T(kq)$	T_{LM}	$T_q^{(k)}$
Clebsch-Gordan coeff.	N/A	$(j'km'q\|j'kjm)$	$\langle J'kM'q\|JM\rangle$	$(kqjm\|kjj'm')$	$C(jLj';mMm')$	$c^{Jkj'}_{mqm'}$
Reduced matrix element	$(\alpha j\|\|T\|\|\alpha' j \pm 1, j)$[b]	$(\alpha j\|\|T^{(k)}\|\|\alpha' j')$	$\langle \tau J\|\|\mathbf{T}^{(k)}\|\|\tau' J'\rangle$	$(\gamma' j'\|\|\mathbf{T}(k)\|\|\gamma j)$	$(j'\|\|T_L\|\|j)$	$\langle J'\|\|T^{(k)}\|\|J\rangle$
Relation to others	See Eq. (30) in [48]	$= \frac{\sqrt{2j+1}}{(-1)^{2k}} R$	$= \frac{\sqrt{2J+1}}{(-)^{2k}} R$	$= \frac{(2j'+1)^{1/2}}{(-1)^{k-j+j'}} R$	$\equiv R$	$= R$

[a]This notation is an adaptation of the notation from [34].
[b]In place of || Condon and Shortley use a set of four vertical dots.

Applying Eqs. (3.17a) and then (3.16a) from [38] for the symmetry properties of the Clebsch-Gordan coefficients to $c^{F',1,F}_{m+q,-q',m+q-q'}$, we find

$$c^{F',1,F}_{m+q,-q',m+q-q'}(-1)^{F'-F}\sqrt{\frac{2F'+1}{2F+1}} = (-1)^{-q'} c^{F,1,F'}_{m+q-q',q',m+q}. \tag{A5}$$

With this, the expression for the spherical components of the atomic polarizability tensor components simplifies to

$$\hat{\alpha}_{q',q} = (-1)^{1-q'} \sum_{F',m} \left[\frac{1}{\hbar \Delta_{F'F}} c^{F,1,F'}_{m+q-q',q',m+q} c^{F,1,F'}_{m,q,m+q} \times |\langle F'||d||F\rangle|^2 |F,m+q-q'\rangle\langle F,m| \right]. \tag{A6}$$

To express the reduced dipole matrix element in the coupled ($F = I + J$) basis in terms of the reduced dipole matrix element in the uncoupled (J) basis, we use Eq. (6.25) from [38] to obtain

$$\begin{aligned}\langle F'||d||F\rangle &= \langle F', J', I||d||F, J, I\rangle \\ &= (-1)^{I+1-J-F}\sqrt{(2J'+1)(2F+1)} \\ &\quad \times W(JFJ'F'; I1)\langle J'||d||J\rangle.\end{aligned} \tag{A7}$$

Here, $W(JFJ'F'; I1)$ is the Racah W coefficient defined in [48]. Expressed in terms of the six-J symbol using Eq. (C.30) from [49], and using the symmetry relations for the six-J symbol (also given in [49]), it is

$$W(JFJ'F'; I1) = (-1)^{-J-F-F'-J'} \begin{Bmatrix} F' & I & J' \\ J & 1 & F \end{Bmatrix}. \tag{A8}$$

Plugging this into the expression for the polarizability tensor components, we obtain

$$\begin{aligned}\hat{\alpha}_{q',q} &= (-1)^{1-q'} \sum_{F'} \left[\frac{1}{\hbar \Delta_{F'F}} |\langle J'||d||J\rangle|^2 \right. \\ &\quad \times (2J'+1)(2F+1) \left| \begin{Bmatrix} F' & I & J' \\ J & 1 & F \end{Bmatrix} \right|^2 \\ &\quad \times \sum_m \left(c^{F,1,F'}_{m+q-q',q',m+q} c^{F,1,F'}_{m,q,m+q} \right. \\ &\quad \left. \left. \times |F,m+q-q'\rangle\langle F,m| \right) \right].\end{aligned} \tag{A9}$$

With the definitions of the relative oscillator strength $f_{F'F}$ [see Eq. (5)] and the characteristic polarizability scalar $\alpha_{0,F'F}$ [Eq. (6), note that the negative sign is absorbed into this definition], and using $(-1)^{-q'} = (-1)^{q'}$ for integer values of q', this becomes

$$\begin{aligned}\hat{\alpha}_{q',q} &= (-1)^{q'} \sum_{F'} \left[\alpha_{0,F'F} f_{F'F} \sum_m \left(c^{F,1,F'}_{m+q-q',q',m+q} c^{F,1,F'}_{m,q,m+q} \right. \right. \\ &\quad \left. \left. \times |F,m+q-q'\rangle\langle F,m| \right) \right],\end{aligned} \tag{A10}$$

as shown in Eq. (4). This is identical to Eq. (6) from [34] except for a factor of $(-1)^{q'}$ instead of (-1), which must be taken into account in configurations with multiple beams at an angle, as there can be a π polarization component (i.e., $q' = 0$) to the electric field.

APPENDIX B: REDUCED DIPOLE MATRIX ELEMENT CONVENTIONS AND CONVERSIONS

When calculating the trapping potential energies in SI units (e.g., for comparison to experiment), care must be taken regarding normalization conventions and units for the reduced dipole matrix element. There are three common conventions for reduced matrix elements. The first convention is that used by Condon and Shortley [47]. When calculating the matrix element of a rank 1 tensor, Condon and Shortley write the factors of the Clebsch-Gordan coefficients that depend on the magnetic substates explicitly but absorb all other factors, including the angular-momentum-dependent factors of the

Clebsch-Gordan coefficients, into the reduced matrix element. This leads to the fact that the normalization factors are different for transitions between different angular momentum states, as shown in [48]. The convention adopted by Racah, as can be seen by combining his Eqs. (16′), (19a), and (29), factors out the Clebsch-Gordan coefficient as well as a factor of $\frac{1}{\sqrt{2J'+1}}$, where J' is the angular momentum of the final state, and a phase factor, or

$$\langle J'm'|T_q^{(k)}|Jm\rangle = (-1)^{2k}\frac{1}{\sqrt{2J'+1}}c_{m,q,m'}^{J,k,J'} \times\langle J'||T^{(k)}||J\rangle_{\text{Racah}}. \quad \text{(B1)}$$

The simplest convention is that adopted by Rose [38], where only the Clebsch-Gordan coefficient is factored out [see Eq. (5.14)], and all other factors are absorbed into the reduced matrix element, yielding

$$\langle J'm'|T_q^{(k)}|Jm\rangle = c_{m,q,m'}^{J,k,J'}\langle J'||T^{(k)}||J\rangle_{\text{Rose}}. \quad \text{(B2)}$$

Thus, the values of the reduced matrix elements are related by

$$\langle J'||T^{(k)}||J\rangle_{\text{Rose}} = (-1)^{2k}\frac{1}{\sqrt{2J'+1}} \times\langle J'||T^{(k)}||J\rangle_{\text{Racah}}. \quad \text{(B3)}$$

Table II summarizes the notations and normalizations employed by different authors.

In this work, we were interested in the reduced matrix elements for dipole transitions. The dipole operator (d) is a tensor of rank $k = 1$, which has three components $q = \pm 1, 0$. The allowed transitions are those with $J' = J + k, J, J - k$, and $m' = m + q$.

When calculating the atomic trapping potential energy using Eq. (6) for the atomic polarizability scalar, care must be taken when using reduced dipole matrix element values from the literature, due to the different normalization conventions as well as units. As this can be nontrivial based on the information given, we present an explicit example here. In an earlier version of our code that still employed Eq. (6) instead of Eq. (7), we used the reduced dipole matrix element from [51], which was given in atomic units, and used the Racah normalization. In order to use this value in our calculation, which uses the Rose normalization, we applied the following conversions:

$$|\langle J'||d||J\rangle_{\text{Rose}}|^2 = \frac{1}{2J'+1} \times|\langle J'||d||J\rangle_{\text{Safronova}}|^2 e^2 a_0^2. \quad \text{(B4)}$$

Here, $\langle J'||d||J\rangle_{\text{Safronova}}$ is the reduced dipole matrix element from [51] (in atomic units), e is the elementary charge, and a_0 is the Bohr radius. Alternatively, Eq. (7) can be used in the calculation, which only requires the laser wavelength of the transition and yields the polarizability scalar in the Rose convention, as needed for our calculation.

APPENDIX C: ELECTRIC FIELDS FOR SINGLE-BEAM AND TWO-BEAM CONFIGURATIONS

To calculate the electric fields for the configurations shown in Sec. III, we started from the electric field distributions determined through Hertz vector diffraction theory [40–42]. The Cartesian components of the electric field (real and imaginary parts) for diffraction of a laser beam incident on a circular aperture at an angle γ was calculated, once for an electric field polarization along the x direction in Figs. 1(a) and 3(a) (s polarization) and once for an electric field polarization perpendicular to the x direction and the direction of propagation (p polarization). The tilted beams with p polarization had both y and z components, although the z components were small since we used only small angles in this study. Each electric field calculation was normalized such that the electric field components were fully extended at time $t = 0$ at the aperture plane, with an electric field magnitude of 1 for the s polarization and also a magnitude of 1 for the p polarization. Six data files were generated for each beam configuration: $\text{Re}(E_{0x})$, $\text{Im}(E_{0x})$, $\text{Re}(E_{0y})$, $\text{Im}(E_{0y})$, $\text{Re}(E_{0z})$, and $\text{Im}(E_{0z})$.

The electric field components were then read into a MATHEMATICA code [44]. At this point, we generated the beam configurations from Sec. III as follows.

For the single-beam configuration, we used a σ^+ polarized beam incident at an angle of $+\gamma$ [see Fig. 1(a)], which we generated by adding an s-polarization component and a p-polarization component, which was lagging behind by a phase of 90°:

$$\mathbf{E}_0 = \frac{1}{\sqrt{2}}[E_{sx}\mathbf{e}_x + i(E_{py}\mathbf{e}_y + E_{pz}\mathbf{e}_z)]. \quad \text{(C1)}$$

Here, E_{sx} is the s-polarization component, and E_{py} and E_{pz} are the p-polarization components along y and z, respectively. Note that all three components are complex, that is, $E_j = \text{Re}(E_j) + i\text{Im}(E_j)$, where $j = sx, py, pz$. The factor of $\frac{1}{\sqrt{2}}$ is to normalize E_0 to 1 at the aperture.

Using Eq. (14) we get the following expressions for the spherical components of the electric field:

$$E_{0-1} = \frac{1}{2}(E_{sx} - E_{py}),$$
$$E_{00} = \frac{i}{\sqrt{2}}E_{pz}, \quad \text{(C2)}$$
$$E_{0+1} = -\frac{1}{2}(E_{sx} + E_{py}).$$

For the two-beam configuration, we added a σ^- beam along the $-\gamma$ direction [see Fig. 3(a)]. This can be achieved either through proper inversion of the s-polarization and p-polarization arrays used for the σ^+ beam or by generating an array specifically for the negative angle. We chose the latter method. This time, the p-polarization component must be ahead of the s-polarization component by a phase of 90°. For this case, we find

$$E_{0-1} = \frac{1}{2}(E_{sx} + E_{py}),$$
$$E_{00} = -\frac{i}{\sqrt{2}}E_{pz}, \quad \text{(C3)}$$
$$E_{0+1} = \frac{1}{2}(-E_{sx} + E_{py}).$$

The total spherical electric field components were the sums of the corresponding electric field components for the σ^+ beam and the σ^- beam.

Once the spherical components of the electric field are determined, they can be plugged into Eq. (11).

[1] G. K. Brennen, C. M. Caves, P. S. Jessen, and I. H. Deutsch, Phys. Rev. Lett. **82**, 1060 (1999).
[2] G. K. Brennen, I. H. Deutsch, and P. S. Jessen, Phys. Rev. A **61**, 062309 (2000).
[3] I. H. Deutsch, G. K. Brennen, and P. S. Jessen, Fortschr. Phys. **48**, 925 (2000).
[4] G. J. Milburn, Fortschr. Phys. **48**, 957 (2000).
[5] D. P. DiVincenzo, Fortschr. Phys. **48**, 771 (2000).
[6] K. Eckert, J. Mompart, X. X. Yi, J. Schliemann, D. Bruß, G. Birkl, and M. Lewenstein, Phys. Rev. A **66**, 042317 (2002).
[7] D. Meschede and A. Rauschenbeutel, Adv. At. Mol. Opt. Phys. **53**, 75 (2006).
[8] M. Karski, L. Förster, J. M. Choi, W. Alt, A. Widera, and D. Meschede, Phys. Rev. Lett. **102**, 053001 (2009).
[9] T. Wilk, A. Gaëtan, C. Evellin, J. Wolters, Y. Miroshnychenko, P. Grangier, and A. Browaeys, Phys. Rev. Lett. **104**, 010502 (2010).
[10] L. Isenhower, E. Urban, X. L. Zhang, A. T. Gill, T. Henage, T. A. Johnson, T. G. Walker, and M. Saffman, Phys. Rev. Lett. **104**, 010503 (2010).
[11] M. Anderlini, P. J. Lee, B. L. Brown, J. Sebby-Strabley, W. D. Phillips, J. V. Porto, Nature (London) **448**, 452 (2007).
[12] R. Dumke, M. Volk, T. Müther, F. B. J. Buchkremer, G. Birkl, and W. Ertmer, Phys. Rev. Lett. **89**, 097903 (2002).
[13] J. Kruse, C. Gierl, M. Schlosser, G. Birkl, Phys. Rev. A **81**, 060308(R), (2010).
[14] S. Bergamini, B. Darquié, M. Jones, L. Jacubowiez, A. Browaeys, and P. Grangier, J. Opt. Soc. Am. B **21**, 1889 (2004).
[15] D. McGloin, G. C. Spalding, H. Melville, W. Sibbett, and K. Dholakia, Opt. Express **11**, 158 (2002).
[16] C. García-Segundo, H. Yan, and M. S. Zhan, Phys. Rev. A **75**, 030902 (R) (2007).
[17] J. Goldwin and E. A. Hinds, Opt. Express **16**, 17808 (2008).
[18] O. Alloschery, R. Mathevet, and J. Weiner, Opt. Express **14**, 12568 (2006).
[19] V. Yannopapas, N. V. Vitanov, J. Phys. Condens. Matter **21**, 245901 (2009).
[20] T. N. Bandi, V. G. Minogin, and S. N. Chormaic, Phys. Rev. A **78**, 013410 (2008).
[21] L. Chen and J. Yin, Phys. Rev. A **80**, 065401 (2009).
[22] K. Christandl, G. P. Lafyatis, S.-C. Lee, and J.-F. Lee, Phys. Rev. A **70**, 032302 (2004).
[23] X. Ji and J. Yin, J. Opt. Soc. Am. B **22**, 1737 (2005).
[24] R. Mu, J. Lu, S. Xu, X. Ji, and J. Yin, J. Opt. Soc. Am. B **26**, 80 (2009).
[25] V. I. Balykin, V. V. Klimov, and V. S. Letokhov, J. Phys. II (France) **4**, 1981 (1994).
[26] V. V. Klimov and V. S. Letokhov, J. Mod. Opt. **42**, 1485 (1995)
[27] V. V. Klimov and V. S. Letokhov, Opt. Commun. **121**, 130 (1995)
[28] V. I. Balykin, V. V. Klimov, and V. S. Letokhov, JETP Lett. **78**, 8 (2003)
[29] V. I. Balykin, V. V. Klimov, and V. S. Letokhov, Opt. Photonics News **16**, 44 (2005).
[30] V. V. Klimov, S. K. Sekatskii, and G. Dietler, Opt. Commun. **259**, 883 (2006)
[31] W. S. Bakr, J. I. Gillen, A. Peng, S. Fölling, and M. Greiner, Nature (London) **465**, 74 (2009).
[32] G. D. Gillen and S. Guha, Am. J. Phys. **72**, 1195 (2004).
[33] G. D. Gillen, S. Guha, and K. Christandl, Phys. Rev. A **73**, 013409 (2006).
[34] I. H. Deutsch and P. S. Jessen, Phys. Rev. A **57**, 1972 (1998).
[35] R. Grimm, M. Weidemüller, and Y. B. Ovchinnikov, Adv. At. Mol. Opt. Phys. **42**, 95 (2000).
[36] I. H. Deutsch and P. S. Jessen, Opt. Commun. **283**, 681 (2010).
[37] J. M. Geremia, J. K. Stockton, and H. Mabuchi, Phys. Rev. A **73**, 042112 (2006).
[38] M. E. Rose, *Elementary Theory of Angular Momentum* (John Wiley & Sons, New York, 1957), p. 88.
[39] P. S. Jessen and I. H. Deutsch, Adv. At. Mol. Opt. Phys. **37**, 95 (1996).
[40] G. Bekefi, J. Appl. Phys. **24**, 1123 (1953).
[41] S. Guha and G. D. Gillen, Opt. Express **13**, 1424 (2005).
[42] For information regarding the MATHCAD code used to calculate the electric field distribution behind a circular aperture using Hertz vector diffraction, contact Glen D. Gillen, ggillen@calpoly.edu.
[43] H. J. Metcalf and P. van der Straten, *Laser Cooling and Trapping* (Springer-Verlag, New York, 1999).
[44] For information regarding the MATHEMATICA code used to calculate the potential energy from the electric field using Eq. (11), contact Katharina Gillen-Christandl.
[45] K. Christandl, Ph.D. thesis, The Ohio State University, 2005.
[46] O. Mandel, M. Greiner, A. Widera, T. Rom, T. W. Hänsch, and I. Bloch, Phys. Rev. Lett. **91**, 010407 (2003).
[47] E. U. Condon and G. H. Shortley, *The Theory of Atomic Spectra* (Cambridge University Press, New York, 1935), p. 63.
[48] G. Racah, Phys. Rev. **62**, 438 (1942).
[49] A. Messiah, *Quantum Mechanics* (Dover, Mineola, NY, 1999), p. 573.
[50] A. R. Edmonds, *Angular Momentum in Quantum Mechanics* (Princeton University Press, Princeton, NJ, 1996), p. 75.
[51] M. S. Safronova, C. J. Williams, and C. W. Clark, Phys. Rev. A **69**, 022509 (2004).